Inorganic Chemistry
Article

Inorg. Chem. 2009, 48, 7585–7592 7585
DOI: 10.1021/ic9000889

# Neutron Diffraction Study of the in Situ Oxidation of $UO_2$

**Lionel Desgranges,*[†] Gianguido Baldinozzi,[‡,§] Gurvan Rousseau,[†,⊥] Jean-Claude Nièpce,[∥] and Gilbert Calvarin[‡,§]**

[†]*CEA, DEN, DEC, Centre de Cadarache, 13108 Saint-Paul-lez-Durance, France,* [‡]*Matériaux Fonctionnels pour l'Energie, SPMS CNRS-Ecole Centrale Paris, 92295 Châtenay-Malabry, France,* [§]*CEA/DEN/DANS/DMN/SRMA/LA2M, 91191 Gif-sur-Yvette, France, and* [∥]*ICB, Dept. Interface et Réactivité des Matériaux, UMR CNRS, Université de Bourgogne, 21000 Dijon, France.* [⊥]*Now at SUBATECH Ecole des Mines La Chantrerie 4 rue Alfred Kastler BP 20722 44307 NANTES CEDEX 3 France.*

Received January 16, 2009

This paper discusses uranium oxide crystal structure modifications that are observed during the low-temperature oxidation which transforms $UO_2$ into $U_3O_8$. The symmetries and the structural parameters of $UO_2$, $\beta$-$U_4O_9$, $\beta$-$U_3O_7$, and $U_3O_8$ were determined by refining neutron diffraction patterns on pure single-phase samples. Neutron diffraction patterns were also collected during the in situ oxidation of powder samples at 483 K. The lattice parameters and relative ratios of the four pure phases were measured during the progression of the isothermal oxidation. The transformation of $UO_2$ into $U_3O_8$ involves a complex modification of the oxygen sublattice and the onset of complex superstructures for $U_4O_9$ and $U_3O_7$, associated with regular stacks of complex defects known as cuboctahedra, which consist of 13 oxygen atoms. The kinetics of the oxidation process are discussed on the basis of the results of the structural analysis.

## Introduction

The oxidation of uranium dioxide has been studied for more than 50 years. It was first studied[1] for fuel fabrication purposes and then later on for safety purposes to design a dry storage facility for spent nuclear fuel that could last several hundred years.[2] Therefore, knowledge of the changes occurring during the oxidation process is essential, and a sound prediction of the behavior of uranium oxides requires an accurate description of the elementary mechanisms on an atomic scale. Only the models based on elementary mechanisms should provide a reliable extrapolation of laboratory results over timeframes spanning several centuries. The oxidation mechanism of uranium oxides requires an accurate understanding of the structural parameters of all of the phases observed during the process. It was shown that a $UO_2$ powder sample undergoes three structural phase transitions at 523 K during the oxidation process, leading to the progressive formation of $\beta$-$U_4O_9$ and $\beta$-$U_3O_7$ and, finally, the complete transformation of the sample into $U_3O_8$.[3] The crystal structures of $UO_2$,[4,5] $U_4O_9$,[6] and $U_3O_8$[7] have already been determined by neutron diffraction experiments with compounds synthesized at higher temperature under thermodynamic equilibrium conditions. Most of these compounds present different phases in the temperature range below 570 K. For instance, the $U_3O_8$ unit cell is orthorhombic at room temperature and hexagonal at high temperatures.[8] $\beta$-$U_3O_7$ is a more complex phase because it is not stable from a thermodynamic point of view, and its crystal symmetry and atomic positions are not known yet.[9] Garrido and Nowicki[10] gave a detailed description of different models for the atomic environments in $U_3O_7$ based on polytypes; however, these descriptions are not suitable for a quantitative analysis because they do not describe the space group and the atomic positions. For all uranium oxide phases, it is also important to establish whether the known structures are representative of the ones involved in the oxidation scenario at lower temperatures (below 570 K) under dry storage conditions. Therefore, the structural features of the complete system of

*To whom correspondence should be addressed. E-mail: lionel.desgranges@cea.fr.

(1) See the review and the references therein: McEachern, R. J.; Taylor, P. *J. Nucl. Mater.* **1998**, *254*, 87.
(2) Ferry, C.; Poinssot, C.; Cappelaere, C.; Desgranges, L.; Jegou, C.; Miserque, F.; Piron, J. P.; Roudil, D.; Gras, J. M. *J. Nucl. Mater.* **2006**, *352*, 246.
(3) Rousseau, G.; Desgranges, L.; Nièpce, J. C.; Bérar, J. F.; Baldinozzi, G. *J. Phys. IV Fr.* **2004**, *118*, 127.
(4) Willis, B. T. M. *J. Phys.* **1964**, *25*, 431.
(5) Rouse, K. D.; Willis, B. T. M.; Pryor, A. W. *Acta Crystallogr.* **1968**, *B24*, 117.
(6) Cooper, R. I.; Willis, B. T. M. *Acta Crystallogr.* **2004**, *A60*, 322–200.
(7) Loopstra, B. O. *Acta Crystallogr.* **1964**, *17*, 651.
(8) Loopstra, B. O. *Acta Crystallogr.* **1970**, *B26*, 656–657.
(9) Allen, G. C.; Tempest, P. A. *Proc. R. Soc. London, Ser. A* **1986**, *406*, 325.
(10) Garrido, F.; Ibberson, R. M.; Nowicki, L.; Willis, B. T. M. *J. Nucl. Mater.* **2003**, *322*, 87.


Published on Web 07/10/2009

phases observed during the low-temperature oxidation of uranium dioxide need to be reviewed.

Allen and Holmes[11] described the transformation of $UO_2$ into $U_3O_8$ as a shear mechanism where the original (111) planes in $UO_2$ change their ABC stacking to a simpler stacking of only one kind of layer (A) associated with an increase in the interlayer distance and a change in the O composition of each layer. At present, the structural modifications induced by oxidation at 523 K cannot be completely assessed, since the structural details of the $U_3O_7$ crystalline structure are still missing. The symmetries of the different phases observed during the isothermal oxidation have already been tentatively identified using synchrotron X-ray diffraction.[3] This experiment provided clear evidence that $UO_2$, $U_4O_9$, and $U_3O_7$ might coexist kinetically in the sample. However, the contribution of oxygen atoms to the X-ray scattering factors is much smaller than that of uranium. Therefore, even though the high resolution of these data can give a precise description of the lattice modifications and the change in the sample microstructure (particle size effects and microstrains), the description of the anion sublattice is not very accurate, despite the fact that the key structural changes take place in this sublattice during the sample oxidation.

The parabolic shape of the weight gain curve suggests that the rate of $U_4O_9/U_3O_7$ formation is limited by oxygen diffusion.[12] The weight gain curves were interpreted taking into account only the oxygen diffusion in a single $U_4O_9/U_3O_7$ phase. This assumption requires a sharp interface between $UO_2$ and $U_4O_9/U_3O_7$,[13] and transmission electron microscopy (TEM) observations on irradiated $UO_2$ provide evidence that supports this model because a thin interface between $UO_2$ and $U_4O_9$ (5 nm) was observed.[14] Nevertheless, Rousseau et al. questioned the physical validity of the average $U_4O_9/U_3O_7$ phase,[15] and Poulesquen et al.[16] proposed a more sophisticated model where two different oxygen diffusion coefficients in $U_4O_9$ and $U_3O_7$ are used.

Therefore, high-resolution in situ neutron diffraction experiments were performed to establish a sound model for the oxidation mechanism below 600 K on an atomic scale. Diffraction patterns of $UO_2$ were measured in situ at 483 K. Diffraction patterns were also collected on single-phase samples to check the published structural results and to provide a benchmark for the refinement of the mixed-phase samples.

This paper focuses on the changes in the $UO_2$ structure during oxidation. It provides the first comprehensive description of the atomic-scale changes in the $UO_2$ structure during oxidation. More specifically, the structure of $\beta$-$U_3O_7$ has been determined and refined.

The paper is divided into two parts. The first part describes the structural features determined in single-phase samples and outlines the structural relationships between these phases. The second part describes the refinement of the diffraction patterns obtained during the in situ experiment, before discussing the quantitative analysis of the phases obtained and the related oxidation mechanism.

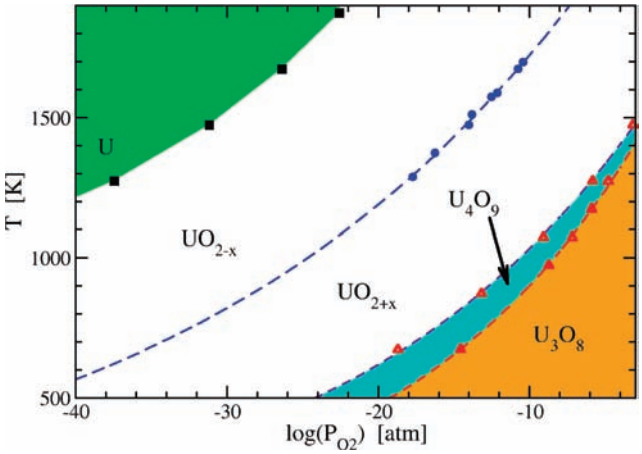


**Figure 1.** Schematic phase diagram showing the domains of the different phases in the $UO_{2+x}$ system as a function of the temperature, $T$, and oxygen partial pressure, $P_{O2}$. The black squares correspond to experimental measurements described in ref 18, whereas the circles correspond to ref 19 and the triangles to ref 20.

## Structural Analysis of Single-Phase Samples

The diffraction pattern of these phases was refined using the JANA program.[17] The refinement results are given in Tables 1−4 in the Supporting Information.

**Sample Synthesis.** $UO_2$, $U_4O_9$, $U_3O_7$, and $U_3O_8$ single-phase samples were synthesized from the same $UO_2$ pellets. The $U_3O_8$ powder was obtained via isothermal annealing at 900 K of the $UO_2$ pellet in dry air. The powder batch was previously characterized in ref 3 using synchrotron radiation: its average grain size was less than 10 $\mu$m, and the size distribution showed normal narrow dispersion. $UO_2$ was prepared at a high temperature (1300 K) by annealing a uranium dioxide powder sample in a gas flow with the correct amount of Ar and $H_2$, making it possible to set the oxygen partial pressure according to Figure 1. To prepare $U_4O_9$, the $UO_2$ powder sample was first maintained at 1270 K for 30 days and slowly cooled down to room temperature for another 12 h. The gas mixture was changed slightly during cooling to maintain the thermodynamic conditions corresponding to the $U_4O_9$ composition. The composition was checked by X-ray diffraction prior to conducting the neutron diffraction experiments. The resulting powder contained less than 1% $U_3O_8$, assuming that the $U_4O_9$ phase in the sample had an oxygen composition that was very close to the phase stability limit in the phase diagram. $U_3O_7$ is not a stable phase at thermodynamic equilibrium;[1] it is therefore not possible to produce a single-phase sample controlling an equilibrium oxygen partial pressure. $U_3O_7$ can only be obtained by quenching a sample of $UO_2$ during oxidation and only at $T < 570$ K. Our previous experiment performed at ESRF[3] on the same batch of powder demonstrated that single-phase $U_3O_7$ can be produced by oxidizing our $UO_2$ sample in dry air for about 7 h at 523 K. Therefore, $U_3O_7$ was synthesized in situ during the oxidation experiment.

**Uranium Dioxide ($UO_2$).** The reference diffraction pattern was measured at room temperature before starting the in situ

(11) Allen, G. C.; Holmes, N. R. *J. Nucl. Mater.* **1995**, *223*, 231.
(12) Aronson, S.; Roof, R. B.; Belle, J *J. Chem. Phys.* **1957**, *27*, 137.
(13) McEachern, R. J. *J. Nucl. Mater.* **1997**, *245*, 238.
(14) Thomas, L. E.; Einziger, R. E.; Buchanan, H. C. *J. Nucl. Mater.* **1993**, *201*, 310.
(15) Rousseau, G.; Desgranges, L.; Charlot, F.; Millot, N.; Nièpce, J. C.; Pijolat, M.; Valdivieso, F.; Baldinozzi, G.; Bérar, J. F. *J. Nucl. Mater.* **2006**, *355*, 10.
(16) Poulesquen, A.; Desgranges, L.; Ferry, C. *J. Nucl. Mater.* **2007**, *362*, 402.
(17) Petricek, V.; Dusek, M.; Palatinus, L. *JANA 2000, The Crystallographic Computing System*: Institute of Physics: Praha, Czech Republic, 2000.
(18) Hagemark, K.; Broli, M. *J. Inorg. Nucl. Chem.* **1966**, *28*, 2837.
(19) Ruello, P.; Petot-Ervas, G.; Petot, C.; Desgranges, L. *J. Am. Ceram. Soc.* **2005**, *88*, 604.
(20) Saito, Y. *J. Nucl. Mater.* **1974**, *51*, 112.

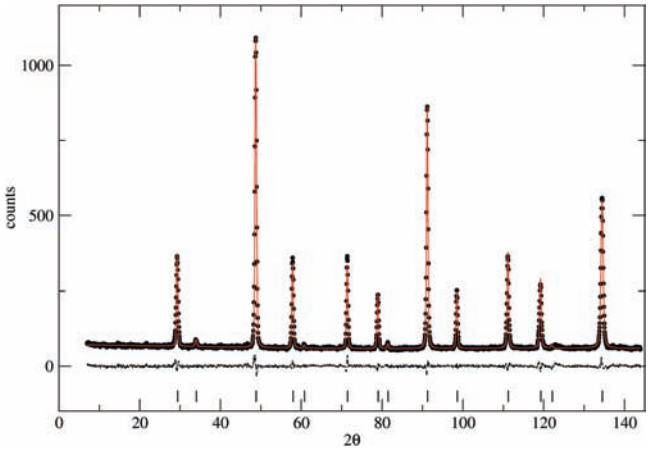


**Figure 2.** Neutron diffraction of $UO_2$ phase at 293 K. The experimental data (dots), the refined profile (red), and the difference profile (black) are displayed. The vertical dashes at the bottom mark the peak positions.

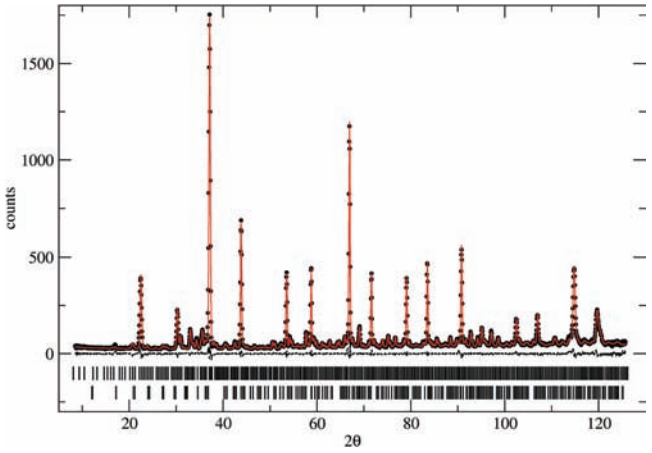


**Figure 3.** Neutron diffraction pattern of $U_4O_9$ phase (dots) compared with its curve fitted by Rietveld analysis (straight line). The difference curve is represented underneath. The sample also contained a few percent of the $U_3O_8$ phase, which was also fitted but did not significantly alter the $U_4O_9$ diffraction pattern.

oxidation experiment, using the same experimental setup (D2b diffractometer at the Institute Laue Langevin (ILL), Grenoble, $\lambda = 1.594$ Å, Ge(220) monochromator). The diffraction pattern (Figure 2) was refined using the usual fluorite crystalline structure (space group *Fm*3*m*).[5] The structure (Table 1, Supporting Information) consists of a simple cubic array of O atoms where U atoms occupy the center of alternate cubes. Therefore, diagonal planes including the centers of cubes containing no cations are planes of weakness, accounting for the excellent octahedral cleavage of fluorite. In this structure, all of the U atoms are 8-fold coordinated with neighboring O atoms. The U−O bond length is 2.368(1) Å, which corresponds to a bond valence sum (BVS)[21,22] of 4.007 for the U atom (with $R_{U-O} = 2.112$ Å and $b = 0.37$ Å). This result confirms the initial stoichiometry of the sample.

**$U_4O_9$.** The neutron diffraction experiment was performed using the 3T2 diffractometer at LLB, Saclay ($\lambda = 1.2251$ Å). The sample was put in a vanadium sample holder, and the diffraction pattern was measured at 400 K using a cryo-furnace.

The diffraction pattern (Figure 3) consists of several main peaks representing the ideal fluorite structure of $UO_2$, and of

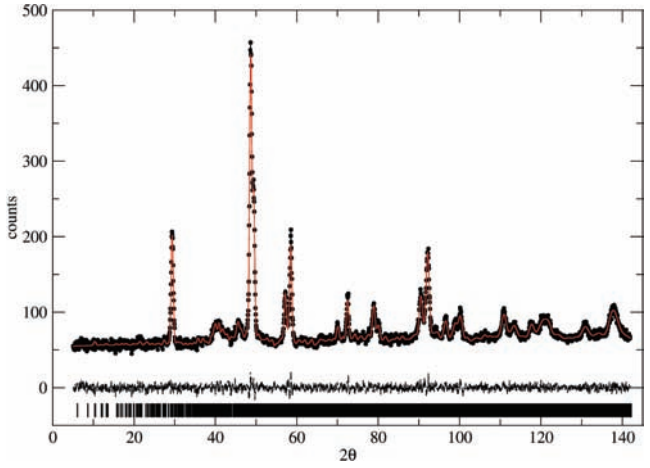


**Figure 4.** Neutron diffraction pattern of the $U_3O_7$ phase (dots) compared with its curve fitted by Rietveld analysis (straight line). The difference curve is represented underneath.

weaker superstructures related to the large supercell obtained by quadrupling of all the $UO_2$ fluorite cell edges, which had already been proposed in the pioneering work by Bevan et al.[23] Recently, Cooper and Willis[6] refined the $U_4O_9$ crystal structure using additional local symmetry restraints stronger than those implied by the space group symmetry ($I\bar{4}3d$). We refined the powder diffraction pattern without applying these restraints, and the refinement converged to reach a very satisfactory solution (Table 2, Supporting Information). A split atom model with statistical occupancies (1/4) for the O atom at the cuboctahedron center (O14; given in Table 2, Supporting Information) provides a better description of the topological disorder affecting this atom. The thermal displacement parameter for this atom is large even in the split-atom model, witnessing its anharmonic behavior.

As also shown in other analyses of the $U_4O_9$ structure,[24,25] the main structural features are related to the existence of oxygen cuboctahedra. Their arrangement gives rise to the different U environments in the structure. There are three kinds of U environments: The first is characteristic of U1, U2, and U3 atoms and corresponds to the 8-fold coordination with O as in the original fluorite structure. The oxygen environments of these atoms are not directly affected by the cuboctahedra. The small polyhedron contraction is responsible for the increase in the uranium BVS. The U4 and U5 atoms are 9-fold coordinated with O atoms. Four bonds have a square face of the cuboctahedron, while the other four with O atoms belong to the original anion sublattice of the fluorite structure. These U atoms are the closest to the cuboctahedra. The local environment is well-described by a square antiprism (as displayed in the top panel of Figure 9) with an additional atom (O14 inside the cuboctahedron) forming the ninth bond (a long bond at about 2.8 Å). These U atoms exhibit the largest increase in their BVS. The remaining uranium atoms (U6 and U7) are 10-fold coordinated with their neighboring O atoms. Three of the bonds (the longest ones) are with the atoms at the triangular surfaces of the cuboctahedron; the remaining seven with atoms are those sitting in the original fluorite sublattice positions. The BVS for these atoms decreased, which is in agreement with Pauling's considerations for atom valences (we used $R_{U-O} = 2.075$ Å and $b = 0.37$ Å for these bond valence sums).

(21) Brown, I. D.; Altermatt, D. *Acta Crystallogr.* **1985**, *B41*, 244.
(22) Brese, N. E.; O'Keeffe, M. *Acta Crystallogr.* **1991**, *B47*, 192.
(23) Bevan, D. J. M.; Grey, I. E.; Willis, B. T. M. *J. Solid State Chem.* **1986**, *61*, 1.
(24) Higgs, J. D.; Thompson, W. T.; Lewis, B. J.; Vogel, S. C. *J. Nucl. Mater.* **2007**, *366*, 297–305.
(25) Garrido, F; Hannon, A. C.; Ibberson, R. M.; Nowicki, L; Willis, B. T. M. *Inorg. Chem.* **2006**, *45*, 8408–8413.

**$U_3O_7$.** The neutron diffraction pattern was measured in situ on the D2b diffractometer at ILL (Figure 4) during the isothermal oxidation experiment at 483 K (see the next paragraph for details). The experimental diffraction pattern exhibits characteristic tetragonal distortion of the main peaks corresponding to the $UO_2$ fluorite structure. Significant changes in the intensities of the 4-fold superstructure peaks are also observed, implying that a significant change in the cuboctahedra stacking is expected, though the average structure is derived from fluorite as it was for $U_4O_9$. No crystalline structure is proposed for the different forms of $U_3O_7$ in the available literature. We established the compatibility relations between the fluorite space group and the 4-fold lattice in a similar manner to the one used by Bevan et al. for building a structural model for $U_4O_9$.[23]

In this approach, we assumed that the tetragonal symmetry of $U_3O_7$ was mainly related to the distortion of the fluorite structure imposed by the cuboctahedra and not related to the stacking of the cuboctahedra as previously proposed by Nowicki et al. in their polytypic analysis.[10] The oxygen content is higher in $U_3O_7$. Therefore, it was reasonable to assume that the $U_3O_7$ crystalline structure involved a larger number of cuboctahedral oxygen clusters. In $U_3O_7$, 16 cuboctahedra (each made of 13 O atoms) must be set in the 4-fold cell to produce a stoichiometry ($U_{256}O_{592} = UO_{2.3125}$) close to the desired one. Three candidate structures can be easily found, each one differing for the center positions of the 16 cuboctahedra. The tetragonal space group with the highest symmetry compatible with these three structures is $I\bar{4}2d$. The three models have 57, 60, or 56 independent atoms. Only the model with 60 independent atoms showed good agreement with the experimental diffraction pattern. In the early stages of the refinement, only the geometry of the cuboctahedra was refined. The main change during this step was the increase in the tilt of the cuboctahedra from their initial orientation (faces parallel to the ones in the $U_4O_9$ structure). All of the structural parameters were refined together in the following steps. Since an apparent 4-fold symmetry was observed for the atoms in the cuboctahedron and the U atoms closer to them, this constraint was imposed during the refinement to reduce the number of parameters. The results of the $\beta$-$U_3O_7$ refinement are summarized in Table 3, Supporting Information. The atom at the center of the cuboctahedron is O0a. The 12 O atoms describing the cuboctahedron surface (displayed in yellow in Figure 9) are labeled O1a−h and O2a−d, while the U atoms forming the shortest bonds with them are labeled U1 (t for the one on top, b for the one at the bottom of the cuboctahedron, and e for four bonds in equatorial positions). The thermal displacement parameters of all of the atoms are smaller than 0.012 Å, with the larger values corresponding to the atoms in the cuboctahedron. The atomic environments are less regular than the ones observed in $U_4O_9$. The main difference between $U_4O_7$ and $U_3O_7$ (see Figure 5) is that the insertion of 16 cuboctahedra in the large cell cannot be done without sharing some oxygen atoms between the deformed square antiprisms surrounding the cuboctahedra (Figure 9). The nature of these contacts and the atomic environments are discussed below.

**Triuranium Octoxide ($U_3O_8$).** Single-phase neutron diffraction patterns were measured on the 3T2 diffractometer ($\lambda$ = 1.2268 Å) at LLB at 533 K (Figure 6).

The structure of $U_3O_8$ was refined using both the orthorhombic and the hexagonal space group already proposed in the literature.[8] Even if the diffraction patterns are collected on a high-resolution diffractometer, the intrinsic broadening of the peaks prevents the direct observation of orthorhombic splitting. Very good reliability factors can be obtained using the orthorhombic model with isotropic profile broadening, or the hexagonal model using the profile broadening according to Stephen's model[26] displaying a significant component acting on hk0 reflections. The reliability factors are slightly better in the hexagonal model where only one independent U atom is needed. We chose to describe $U_3O_8$ within the hexagonal model; this choice is more appropriate for describing the modifications occurring in the $UO_2$ structure during oxidation. The results of the Rietveld refinement are summarized in Table 4, Supporting Information. The O1 atom forms the shortest bonds (2.077 Å) with U and is responsible for interlayer cohesion. Two independent U atoms exist in the orthorhombic space group, but they do have similar environments (the short bonds in the interlayer are the same) and similar bond valence sums (5.08 and 5.36).

**Crystallographic Relations between $UO_2$ and α-$U_3O_8$ via $\beta$-$U_4O_9$ and $\beta$-$U_3O_7$.** These structural refinements provide accurate models for uranium oxide structures from $UO_2$ to $U_3O_8$, making it possible to follow the structural modifications occurring during oxidation on an atomic level. These structures provide a benchmark for the refinement of the diffraction

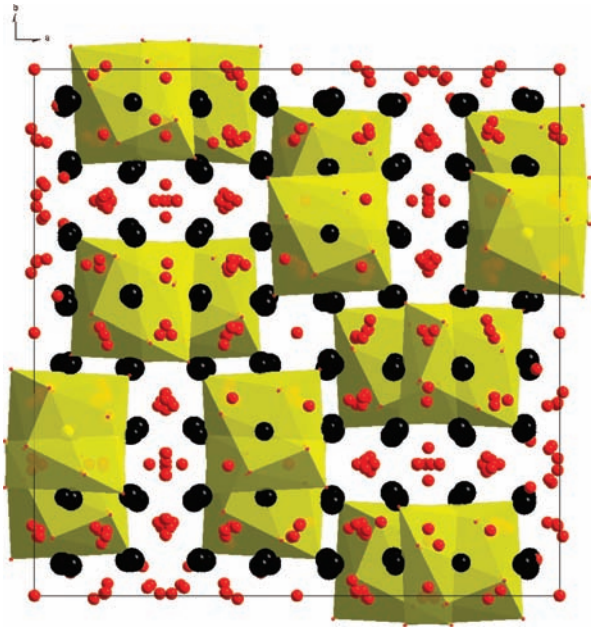

**Figure 5.** Structural model for the $\beta$ phase of $U_3O_7$ (oxygen atoms in red, uranium atoms in black). The 16 cuboctahedra are now tilted and deformed, possibly because of their stronger mutual interactions.

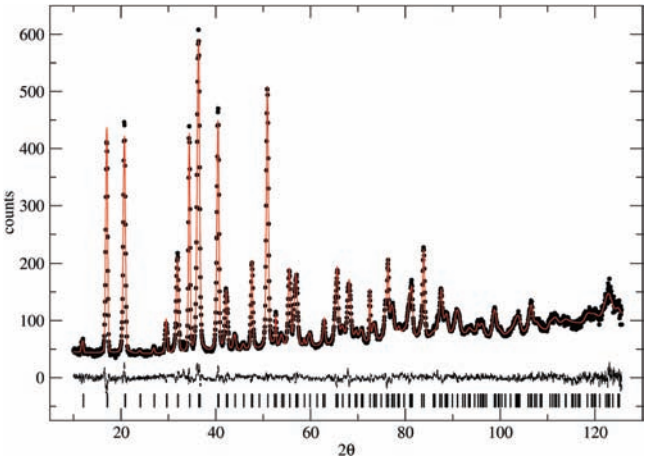


**Figure 6.** Neutron diffraction pattern of $U_3O_8$ phase (dots) compared with its curve fitted by Rietveld analysis (straight line). The difference curve is represented underneath.

(26) Stephens, P. W. *J. Appl. Crystallogr.* **1999**, *32*, 281.

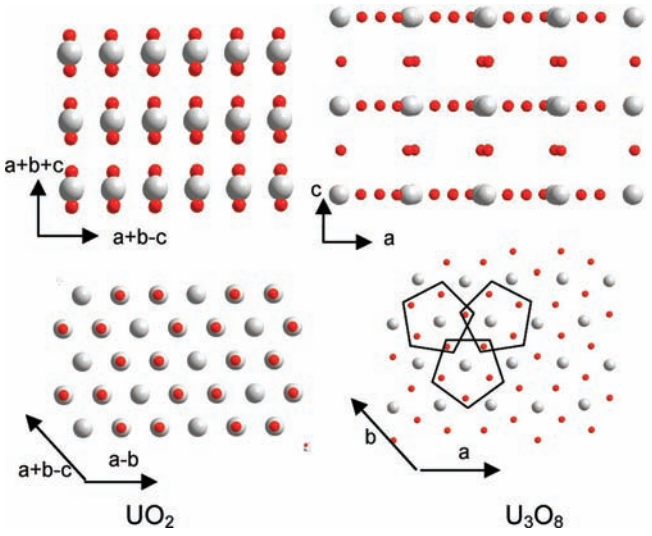


**Figure 7.** Projection of the $UO_2$ (left) and $U_3O_8$ (right) crystalline structures on two planes, showing their similarities and differences (see text for details).

patterns obtained during the isothermal oxidation where several phases coexist in the sample.

Although they have different space groups, these uranium oxides share several similarities. This is especially true when we look at a structure such as the stacking of (111) layers. This point will be illustrated, first, by recalling the crystalline relationships between $UO_2$ and $U_3O_8$ proposed by Allen and Holmes,[11] in which these dense planes are significant.

The $UO_2$ structure is based upon the close packing of ions into hexagonal layers perpendicular to the main diagonal of the fluorite cell. Each layer contains only one kind of atom: either U or O. These hexagonal layers are stacked in an ABC fashion, so that the fourth layer lies immediately over the first and so forth. The regular ABC stacking of hexagonal layers consisting of alternate elements gives rise to the rock salt structure. Half of the U layers are missing in $UO_2$, which is a fluorite structure.

Despite the different chemical formulas, the hexagonal U sublattice in $U_3O_8$ is very similar to that in the $UO_2$ fluorite structure, which means topotactic growth is thus possible. The hexagonal (or orthorhombic) (001) planes of $U_3O_8$ oxide can efficiently grow on the (111) layers of $UO_2$. Nevertheless, the structural matching between (111) planes in the fluorite structure and the (001) planes in $U_3O_8$ is limited to the U sublattice, as shown in Figure 7. Moreover, the stacking sequence of the (001) planes in $U_3O_8$ consists of only a single kind of repetitive layer (A). The main differences between the two structures arise from the anion arrangement. While all of the O atoms lie in separate layers in $UO_2$, most of the O atoms sit in the same U layer in $U_3O_8$, thus creating a pentagonal pattern around each U atom. A limited number of O atoms still sit in the interlayer on top of each U atom, creating pillars that connect these layers. These U−O−U bonds are shorter than the U−O bonds in $UO_2$ (2.077 instead of 2.368 Å), and they form the height of pentagonal bipyramids. Regardless of whether the U−O bonds in the interlayer are short, the distance between two U layers is now larger than in $UO_2$ (4.152 instead of 3.157 Å). It is responsible for most of the volume increase observed during the phase transformation from $UO_2$ to $U_3O_8$ (from 40.9 to 55.8 $Å^3$ for a volume containing one uranium atom). However, U−U distances in the layer are not much longer (Figure 7) than those in $UO_2$, though the O atoms now share this same layer.

The description of the $U_4O_9$ and $U_3O_7$ structures can shed some light on the structural changes affecting the anion sublattice occurring during oxidation. The incorporation of oxygen

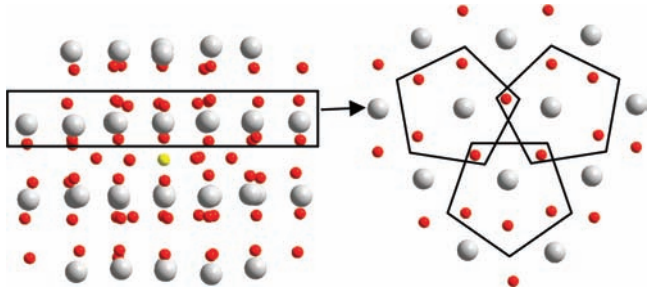

**Figure 8.** Left: Projection in the $(a+b+c\,;a+b-c)$ plane of the $U_4O_9$ crystalline structure around a cuboctahedron (the oxygen at the center of the cuboctahedron is in yellow). Right: Projection of the section taken from the left image (represented by a black rectangle) in the $(a+b-c;$ $a-b)$ plane. The pentagonal arrangement of the oxygen atom is similar to the one evidenced in $U_3O_8$ in Figure 7.

cuboctahedra in the $UO_2$ structure starts the deep modification of the anion sublattice. The main structural feature of the $U_4O_9$ structure is the existence of 12 cuboctahedra, each made of 13 O atoms: six neighboring U atoms, sharing the normal cation sublattice of the fluorite structure, reveal square antiprism coordination instead of the normal cubic coordination. The interstitial O atoms describing the cuboctahedron faces deplete the anion sites in the fluorite structure, and they introduce new O atom layers closer to the U layers. In contrast, the atoms at the center of the cuboctahedra lie midway between two U layers, in a position in which it is possible to identify with the O atoms forming the pillars connecting the layers in the $U_3O_8$ structure. When a thick slab formed by a U layer and the new O atom layers consisting of interstitial O atoms are projected along ⟨111⟩, this projected slab is already very similar to the pentagonal pattern existing in the $U_3O_8$ structure (Figure 8). Therefore, the formation of cuboctahedra starts to produce some of the structural features responsible for the larger structural modifications occurring in $U_3O_8$.

When $U_3O_7$ is formed, 16 cuboctahedra, which are noticeably tilted and deformed (Figure 5), are incorporated into the fluorite structure. It is important to point out that none of the 16 cuboctahedra in $U_3O_7$ are found in the same position in the 12 cuboctahedra for $U_4O_9$. This fact reveals the great mobility of O atoms in these structures. Therefore, the O sublattice is efficiently reorganized via the creation and destruction of cuboctahedra. In $U_4O_9$, none of the atoms of the square antiprisms surrounding the cuboctahedra are shared (top panel of Figure 9). However, the 16 cuboctahedra in $U_3O_7$ cannot be efficiently distributed in the unit cell, preventing the mutual sharing of some of the O atoms defining the square antiprisms. Three different types of contacts exist between these units in $U_3O_7$ (bottom panel of Figure 9). In the first type of contact, U1b and U1t in the square antiprisms shift toward each other; they form short U−O bonds with the two oxygen atoms of the shared edge. These short U−O distances ($< 2.1$ Å) are compatible with an O−U−O uranyl group, but in our case, it forms an angle that is much smaller than 180°, as in a uranyl group. These short bonds are responsible for the large increase in the BVS of U1t and U1b atoms (Table 3, Supporting Information) compared with the values of the corresponding U atoms in the $U_4O_9$ structure (U4 and U5 in Table 2, Supporting Information). The second and third types of contacts do not involve such a strong distortion of the square antiprisms, but they still generate short U−O bonds between the atoms in the fluorite positions close to the contact edges. These shorter bonds are responsible for the large increase in the BVS of U5c and O15b.

These short U−O bonds induced both inside and outside the cuboctahedra are mainly associated with the tetragonal distortion of the $U_4O_9$ lattice and the cuboctahedra tilt. In this process, each cuboctahedron loses its 3-fold axis and becomes more elongated along the $c_t$ axis. This elongation is a more

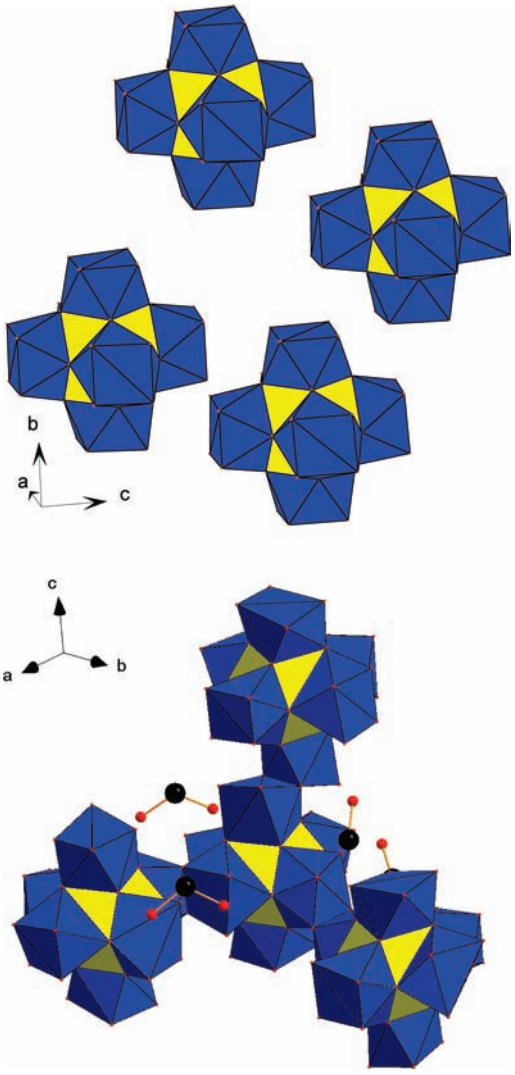


**Figure 9.** Top panel: Relative positions of the yellow cuboctahedra in the $U_4O_9$ structure. Bottom panel: Relative positions of the cuboctahedra with the blue deformed square antiprisms sharing edges in the $U_3O_7$ structure.

pronounced feature for atoms involved in type 1 contacts. The distorted cuboctahedra and the associated shorter U−O bonds are also consistent with the infrared absorption band changes observed in $U_4O_9$ and in $U_3O_7$ phases.[27]

It is important to stress that the metastable nature of $U_3O_7$ implies that it will transform into a mixture of $U_4O_9$ and $U_3O_8$, provided enough time is given to reach thermodynamic equilibrium at the annealing temperature. Therefore, it is not possible to exclude that the cuboctahedron configurations determined in this experiment may be dependent on kinetic parameters. At present, no study has been performed to check whether the structural features of $U_3O_7$ depend on these parameters. The accumulation of local deformations in $U_3O_7$ due to the frustrated environments of the square antiprisms may be incompatible with the long-term existence of the cuboctahedra, and above a given threshold, it may trigger its transformation into $U_3O_8$.

## In Situ Isothermal Oxidation Experiment

**Sample Preparation and Refinement Strategy.** The isothermal oxidation experiment (483 K) was performed on the D2b diffractometer at ILL. The sample was put into a cylindrical vanadium sample holder, and dry air was forced to flow through it to ensure a stable oxidizing atmosphere during the experiment. Since a dense sample would prevent achieving the optimum conditions for the uniform oxidation of the sample, $UO_2$ powder was dispersed in the cylindrical sample holder using fused silica fibers to ensure a dry air flow within the sample. The temperature was measured near the sample, just a few millimeters below the area irradiated by the neutron beam. The oxidation experiment was performed at 483 K (as measured by the thermocouple). The furnace steady state was reached after less than 10 min. Each complete diffraction pattern ($6 < 2\theta < 145$) was recorded for 30 min until a significant fraction of $U_3O_8$ was formed (Figure 10). A preliminary step involved measuring a diffraction pattern of the sample holder only containing the silica fibers. This diffraction pattern was subtracted from all of the diffraction patterns measured during the in situ oxidation. The result of this subtraction was extremely satisfactory, and the statistical quality of each measured point was corrected to take into account this operation. Very small structural changes seem to occur in the range of coexistence of the $U_4O_9$ and $U_3O_7$ phases. Therefore, only a limited number of parameters were refined (relative scale factors, lattice metric, and profile functions), greatly reducing the complexity of the refinement and producing a more robust estimate of the refined parameters. The other parameters were taken from the refinement results of the single-phase diffraction patterns, and they actually produced excellent agreement factors throughout the whole isothermal oxidation experiment ($R_{wp} < 5.5\%$, $R_B < 2.5\%$).

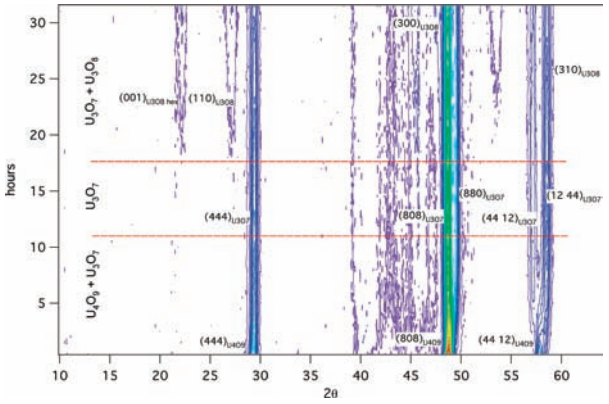


**Figure 10.** Map of the diffracted intensity as a function of the $2\theta$ angle and time during the in situ experiment.

**Results.** The change in the relative phase proportions and the cell parameters of each phase observed during the in situ isothermal experiment are shown in Figures 11 and 12, respectively. $UO_2$ and $U_4O_9$ phases cannot be easily distinguished in our experiment because of a severe overlap of the fluorite basic peaks. A reliable estimate of the relative amounts of $UO_2$ and $U_4O_9$ can be achieved from the Rietveld refinement of the first and second diffraction patterns at the beginning of the oxidation experiment. The amount of $UO_2$ phase in the third diffraction pattern is already very small. For this reason, only the global amount of these two phases is given instead of their

(27) Allen, G. C.; Crofts, J. A.; Griffiths, A. J. *J. Nucl. Mater.* **1976**, *62*, 273.

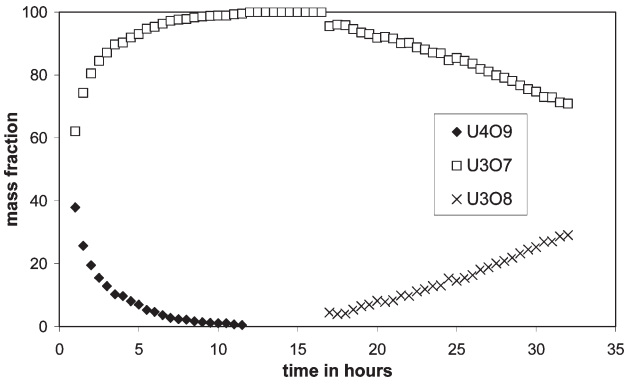


**Figure 11.** Mass fraction of the different phases as determined by Rietveld analysis as a function of time during the in situ experiment.

partial mass fractions. A $U_3O_7$ single phase is observed after about 10 h. $U_3O_8$ formation occurs after about 17 h.

$U_4O_9$ and $U_3O_8$ unit cell parameters display small variations from the value determined in the single-phase diffraction patterns at the same temperature. This result is consistent with the equilibrium phase diagram that predicts biphasic regions with limiting phases having very small departures from stoichiometry ($U_4O_{9-y}$ and $U_3O_{8-z}$). The initial buildup of $U_3O_7$ clearly displays a significant increase in the tetragonal distortion, as long as a significant amount of $U_4O_9$ phase is present in the sample. This effect does not seem to be related to a change in the stoichiometry of the $U_3O_7$ phase but rather to the mutual strain produced by the topotactic growth of $U_3O_7$ on top of $U_4O_9$. During this buildup, a strain relaxation mechanism progressively occurs as $U_4O_9$ disappears.

## Discussion

The phase diagram of the UO system is the subject of various recent papers. Recently, Andersson et al.[28] performed ab initio calculations to investigate the possible point defects and the possible clustering that may occur in the composition range $UO_2-UO_{2.25}$. From an experimental viewpoint, Higgs et al. studied a sample with the $UO_{2.17}$ composition as a function of the temperature[24] on the basis of neutron diffraction. Our in situ experiment investigates the UO system at a fixed temperature (483 K), letting the O content increase due to oxidation in the air. It evidenced that the oxidation of $UO_2$ occurs via the formation of $U_4O_9$ before being followed by the formation of $U_3O_7$ and then $U_3O_8$. The crystalline structures of $U_4O_9$ and $U_3O_8$ formed during oxidation at 483 K are the same as those determined on samples fabricated at higher temperatures. These structural data depict the average crystalline structure of these compounds and can hardly be used to discuss the point defects proposed by Andersson et al. Nevertheless, the crystalline structure of the phases determined in reference samples can be used to recommend a mechanistic description of oxidation on an atomic level. This description can be divided into the three following stages by considering the incorporation of cuboctahedra in the $UO_2$ lattice.

**Stage 1.** At the very beginning of oxidation, incorporating oxygen into $UO_2$ results in the formation of cuboctahedra. Various recent first-principle calculations have confirmed that the cuboctahedron is a more stable defect in hyper-stoichiometric $UO_2$ than oxygen interstitials at temperatures below 600 K.[29,30] These calculations are consistent with the fact that no oxygen diffusion profile was observed in $UO_2$, leading to a sharp interface between $U_4O_9$ and $UO_2$.[13,14]

The oxidation reaction can be described by the sequence of elementary steps: oxygen gas molecule adsorption, dissociation, and incorporation in $UO_2$ followed by point defect diffusion and cuboctahedron formation. The oxidation kinetics in this first stage are controlled by the slower elementary step, the so-called rate-limiting step. The transformation kinetics of $UO_2$ into $U_4O_9$ are generally modeled assuming they are controlled by oxygen diffusion.[13] Because of their size, cuboctahedra are not likely to move on their own. The kinetics controlling oxygen diffusion are more likely due to the migration oxygen point defects. There may be either vacancy or interstitial oxygen point defects. Because the oxidation kinetics are mostly insensitive to the oxygen partial pressure,[1] the point defect involved in the rate-limiting step in stage 1 is likely to be oxygen vacancy in $U_4O_9$.

**Stage 2.** Because of oxygen diffusion in $U_4O_9$, an oxygen concentration gradient is formed in the $U_4O_9$ layer created on $UO_2$. This gradient would result in the formation of $U_3O_7$ at the sample surface when an oxygen concentration threshold corresponding to the formation of extra cuboctahedra in $U_4O_9$ has been reached.

Once the cuboctahedra interact with each other and form $U_3O_7$ phases, an additional elementary step has to be added in the description of the oxidation reaction: the dynamic rearrangement of the cuboctahedra. This rearrangement is derived from the oxygen point defect diffusion. Thus, the $U_3O_7$ oxidation kinetics are slower than the $U_4O_9$ kinetics: the diffusion of oxygen point defects is slowed down in $U_3O_7$ because of the dynamic rearrangement of the cuboctahedra. This is consistent with the Poulesquen et al. approach that recommends two different oxygen diffusion coefficients for $U_4O_9$ and $U_3O_7$.[16]

During $UO_2$ oxidation, Bae et al.[31] observed some spalling in a two-step process: macrocracking is first associated with the formation of $U_4O_9$ and $U_3O_7$, and then microcracking is associated with the formation of $U_3O_8$. Macrocracking could be correlated to the change in the $U_3O_7$ unit cell parameter depicted in Figure 12. The mutual strain produced by the topotactic growth of $U_3O_7$ on top of $U_4O_9$ can induce some cracks, provided the resulting stresses reach a threshold value. Therefore, the observed strain relaxation, which progressively occurs as $U_4O_9$ disappears, may be attributed to crack formation.

**Stage 3.** Finally, the formation of $U_3O_8$ possibly takes place when the topological frustration imposed on the (111) dense planes by the cuboctahedra is no longer sufficient to prevent the rearrangement from the ABCA stacking of $U_3O_7$ into the AAA stacking of $U_3O_8$. From a

(28) Andersson, D. A.; Lezama, J; Uberuaga, B. P.; Deo, C; Conradson, S. D. *Phys. Rev.* **2009**, *B 79*, 204110.

(29) Geng, H. Y.; Chen, Y.; Kaneta, Y.; Iwasawa, M.; Ohnuma, T.; Kinoshita, M. *Phys. Rev.* **2008**, *B 77*, 104120.

(30) Geng, H. Y.; Chen, Y.; Kaneta, Y.; Kinoshita, M. *Phys. Rev.* **2008**, *B 77*, 180101.

(31) Bae, K. K.; Kim, B. G.; Lee, Y. W.; Yang; Park, H. S. *J. Nucl. Mater.* **1994**, *209*, 274.

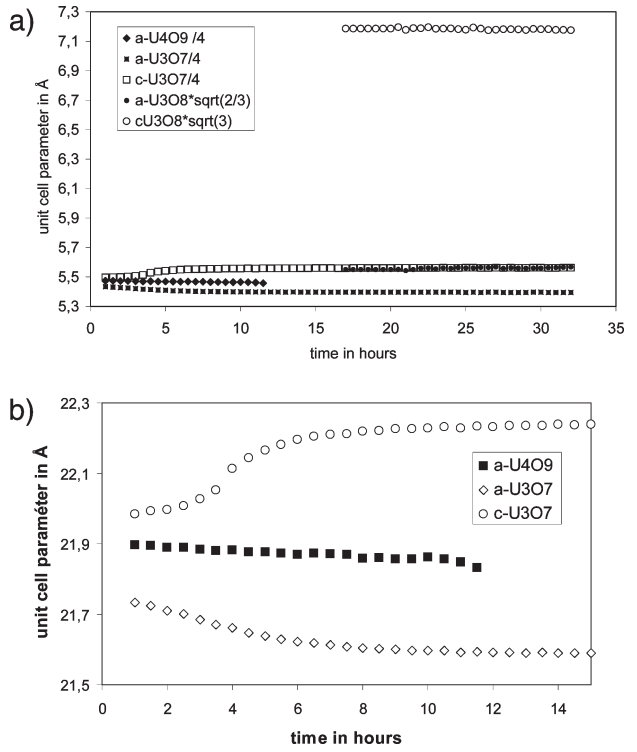


**Figure 12.** (a) Unit cell parameter of the different phases as determined by Rietveld analysis as a function of time during the in situ experiment. (b) Detail of part a showing $U_4O_9$ and $U_3O_7$ unit cells at the beginning of the experiment.

phenomenological viewpoint, this is very similar to a martensitic-type transition.

From a kinetic viewpoint, two main parameters should then control the formation of $U_3O_8$: sufficient oxygen concentration that allows the dynamic rearrangement of the cuboctahedra and ample incubation time needed to achieve sufficient oxygen point defect rearrangement.

This is consistent with a nucleation and growth mechanism, though with faster growth kinetics, as in the case of a martensitic transition. However, the correlation between $U_3O_8$ formation and the weight gain measured during an $UO_2$ oxidation experiment is not straightforward because the cracking in the $UO_2$ sample described in stage 2 has to be taken into account. This point will be discussed in a future paper.

## Conclusion

The results obtained in this study provide a comprehensive structural description of the transformation of $UO_2$ into $U_3O_8$ at temperatures below 700 K. This description is consistent with most of the experimental results available on this system. Moreover, it provides a sound basis for the use of two different oxygen diffusion coefficients in $U_4O_9$ and $U_3O_7$, as recently proposed by Poulesquen et al.[16] The characteristics of $U_3O_7$ are explained by the formation of topological frustrations that modify the regular stacking of the cuboctahedra.

This interpretation supports the similar behavior observed in spent $UO_2$ fuel at temperatures below 570 K. In oxidized irradiated $UO_2$, the $\gamma U_4O_9$ crystalline phase was observed with TEM,[14] but no $U_3O_7$ has been reported so far. This can be interpreted by taking into account irradiation-induced defects that create lattice distortions and may prevent the regular ordering of the cuboctahedra in $UO_2$. Because $U_4O_9$ and $U_3O_7$ result from the ordering of the cuboctahedra over large atomic distances (at least 10−100 nm), their perfect ordering cannot be achieved in irradiated $UO_2$, which adopts a $\gamma U_4O_9$ crystalline structure. $\gamma U_4O_9$ was observed with TEM at high temperatures on unirradiated $UO_2$[32] and corresponds to partially disordered $U_4O_9$. The accumulation of oxygen in $\gamma U_4O_9$ up to a 2.4 O/M ratio could then be interpreted as an increase in the cuboctahedron density in a partially disordered manner.

**Acknowledgment.** The authors are gratefully indebted to F. Bourré (LLB) and Th. Hansen (ILL) for their help in collecting the experimental data, and to G. Petot for the discussions and help in setting up the controlled atmosphere to produce the single-phase sample of $U_4O_9$. The authors would also like to acknowledge financial support from Electricité de France.

**Supporting Information Available:** The refinement results are given in Tables 1−4 for $UO_2$, $U_4O_9$, $U_3O_7$, and $U_3O_8$ respectively. This material is available free of charge via the Internet at http://pubs.acs.org.

(32) Blank, H.; Ronchi, C. *Acta Crystallogr.* **1968**, *A24*, 657.